Sustainable
Energy & Fuels

PAPER

View Article Online
View Journal | View Issue

Cite this: *Sustainable Energy Fuels*, 2023, 7, 3384

Electro- and photochemical H_2 generation by Co(II) polypyridyl-based catalysts bearing *ortho*-substituted pyridines†

Fiorella Lucarini,[a] Jennifer Fize,[b] Adina Morozan,[b] Federico Droghetti,[c] Euro Solari,[d] Rosario Scopelliti,[d] Marco Marazzi,*[ef] Mirco Natali,*[c] Mariachiara Pastore,*[g] Vincent Artero*[b] and Albert Ruggi*[a]

Received 7th March 2023
Accepted 25th May 2023

DOI: 10.1039/d3se00295k

rsc.li/sustainable-energy

Cobalt(II) complexes featuring hexadentate amino-pyridyl ligands have been recently discovered as highly active catalysts for the Hydrogen Evolution Reaction (HER), whose high performance arises from the possibility of assisting proton transfer processes *via* intramolecular routes involving detached pyridine units. With the aim of gaining insights into such catalytic routes, three new proton reduction catalysts based on amino-polypyridyl ligands are reported, focusing on substitution of the pyridine *ortho*-position. Specifically, a carboxylate (**C2**) and two hydroxyl substituted pyridyl moieties (**C3**, **C4**) are introduced with the aim of promoting intramolecular proton transfer which possibly enhances the efficiency of the catalysts. Foot-of-the-wave and catalytic Tafel plot analyses have been utilized to benchmark the catalytic performances under electrochemical conditions in acetonitrile using trifluoroacetic acid as the proton source. In this respect, the cobalt complex **C3** turns out to be the fastest catalyst in the series, with a maximum turnover frequency (TOF) of 1.6 (±0.5) × 10^5 s^{-1}, but at the expense of large overpotentials. Mechanistic investigations by means of Density Functional Theory (DFT) suggest a typical ECEC mechanism (*i.e.* a sequence of reduction – E – and protonation – C – events) for all the catalysts, as previously envisioned for the parent unsubstituted complex **C1**. Interestingly, in the case of complex **C2**, the catalytic route is triggered by initial protonation of the carboxylate group resulting in a less common (C)ECEC mechanism. The pivotal role of the hexadentate chelating ligand in providing internal proton relays to assist hydrogen elimination is further confirmed within this novel class of molecular catalysts, thus highlighting the relevance of a flexible polypyridine ligand in the design of efficient cobalt complexes for the HER. Photochemical studies in aqueous solution using $[Ru(bpy)_3]^{2+}$ (where bpy = 2,2′-bipyridine) as the sensitizer and ascorbate as the sacrificial electron donor support the superior performance of **C3**.

1. Introduction

The production of clean fuels from renewable energy supplies, such as solar energy, is one of the most ambitious scientific challenges, which would provide a solution to the current energy and environmental problems.[1,2] Because of the potential of hydrogen as a green fuel, most of the research has so far been focused on the development of systems for the reduction of protons to generate H_2.[3] In particular, the formation of molecular hydrogen from light-driven water splitting is an attractive strategy to exploit and store the enormous amount of energy contained in solar light.[4–7] Inspired by the ability of nature to

---

[a] Université de Fribourg, Ch. du Musée 9, 1700 Fribourg, Switzerland. E-mail: albert.ruggi@unifr.ch

[b] Univ. Grenoble Alpes, CNRS, CEA, IRIG, Laboratoire de Chimie et Biologie des Métaux, 17 rue des Martyrs, 38000 Grenoble, France. E-mail: vincent.artero@cea.fr

[c] Università degli Studi di Ferrara, Dipartimento di Scienze Chimiche, Farmaceutiche ed Agrarie (DOCPAS) Via L. Borsari 46, 44121 Ferrara, Italy. E-mail: mirco.natali@unife.it

[d] Institut des Sciences et Ingénierie Chimique, École Polytechnique Fédérale de Lausanne (EPFL), 1015 Lausanne, Switzerland

[e] Universidad de Alcalá, Departamento de Química Analítica, Química Física e Ingeniería Química, Grupo de Reactividad y Estructura Molecular (RESMOL), Alcalá de Henares, Madrid, Spain. E-mail: marco.marazzi@uah.es

[f] Universidad de Alcalá, Instituto de Investigación Química "Andrés M. del Río" (IQAR), Alcalá de Henares, Madrid, Spain

[g] Université de Lorraine & CNRS, Laboratoire de Physique et Chimie Théoriques (LPCT), F-54000, Nancy, France. E-mail: mariachiara.pastore@univ-lorraine.fr

† Electronic supplementary information (ESI) available: Detailed synthetic procedures and compounds characterization, electrochemical and photochemical supplementary data, foot of the wave analysis, and crystallographic, spectroscopic and computational data. CCDC 2245266–2245269. For ESI and crystallographic data in CIF or other electronic format see DOI: https://doi.org/10.1039/d3se00295k

convert solar energy into chemical fuels (*i.e. via* the photosynthesis process), photoinduced proton reduction systems need at least three components: a light absorber (*i.e.* photosensitizer), a catalyst and an electron donor.[8] Another promising way to produce H–H bonds is through electrochemical reduction of protons using solar-generated electricity.[9,10] In both cases, the final goal is to obtain highly efficient systems capable of operating under fully aqueous conditions. Nevertheless, electrochemical studies aimed at gaining insights into the performance of the catalysts are generally carried out in organic media, in which the amount of protons can be more precisely controlled.[11] For the development of systems active in both electro- and photochemical hydrogen production, particular attention has been paid to homogeneous molecular catalysts based on abundant, cheap, and noble-metal-free species, such as di-iron hydrogenase mimics or bioinspired cobalt and nickel complexes.[12–21] Cobaloxime complexes, in particular, have emerged as active catalysts for electrochemical proton reduction because of the low overpotential and the high catalysis rate.[22] These complexes have also been employed as catalysts in photochemical systems, although the low stability in fully aqueous media due to ligand exchange and hydrolysis dramatically limits their applicability.[18,19] Recently, polypyridyl cobalt complexes have been reported as competent catalysts, showing excellent stability and impressive activity even though they display higher overpotentials with respect to cobaloximes.[23–25] We have recently reported a polypyridyl cobalt complex having an exotic heptacoordinate structure, which showed outstanding performances in light-driven hydrogen production.[26,27] Synthetic modifications by ligand substitutions enable the optimization of the catalytic properties of this class of catalysts. Indeed, the introduction of electron withdrawing groups (*i.e.* EWG) or electron donating groups (*i.e.* EDG) can affect the reduction potentials of the cobalt centre, while their position can modulate the catalytic mechanism, thus allowing the optimization of the performances.[28,29] In particular, we have recently proved that the position of the substituents plays a more prominent role in the photochemical efficiency towards hydrogen production using $[Ru(bpy)_3]^{2+}$ (where bpy = 2,2′-bipyridine) as the sensitizer,[30] while electronic effects become relevant in the light-driven performance when using less powerful reducing agents.[31] Several research groups have also performed the functionalization with carboxylic or hydroxyl groups in peripheral positions with respect to the metal centre in order to promote intramolecular proton transfer, thus enhancing the efficiency of the catalysis.[32] In the same vein, Zonta, Natali and co-workers[33] introduced different substituents (*i.e.* –OH, $-CH_2OH$, –CHO, $-CONH_2$) on the phenyl ring of an amino polypyridine cobalt complex, in order to modify the solvent–ligand interactions without affecting the electronic properties of the metal centre. The authors observed, however, only small differences in the efficiency among the considered complexes. In particular, they attributed the slightly higher activity of the complexes bearing –OH and $-CH_2OH$ to the presence of the hydroxyl group that could promote the formation of a H-bonded water network near the cobalt. Conversely, the low performances of the catalysts bearing –CHO and $-CONH_2$ were ascribed to a lower stability of the catalysts induced by these substituents. Herein, we present the synthesis and the characterization of three new amino-polypyridyl cobalt complexes bearing different functional groups *i.e.* $-CO_2^-$, $-CH_2OH$ and –OH (yielding **C2**, **C3**, and **C4** respectively) in the *ortho*-position to the N of the pyridine moiety with the aim of studying their effect on the catalytic activity in the electrochemical and photochemical hydrogen production.[26] The presence of such substituents is expected to actively influence the role of the pyridine group in assisting the protonation of the metal centre, thus affecting the overall catalysis. The rate constants of the protonation steps are extrapolated from electrochemical studies in acetonitrile with trifluoroacetic acid (TFA) as proton source. Experiments of photoinduced H_2 evolution in water are performed in the presence of ascorbic acid as electron donor and $[Ru(bpy)_3]^{2+}$ as sensitizer. Density Functional Theory (DFT) was employed to calculate the relative stability and structure of the intermediates involved in H_2 production, including those in the final H_2 release, making possible a comparison between different pathways for each proposed compound and allowing a reliable rationalization of the experimental results.

2. Methodology

2.1 Synthesis and characterization

The synthesis of the compounds was performed according to the procedure reported in Section S2 of the ESI.† Solid state structures were obtained by X-ray diffraction on single crystals prepared by slow diffusion of diethyl ether into methanolic solutions of the complexes.

To observe possible variations of the electronic absorption of the catalysts in the presence of a source of protons, UV-Vis spectra were measured in 4 mM solutions of complexes in CH_3CN in the presence of increasing amounts of trifluoroacetic acid (TFA) by keeping the final volume (2 mL) unchanged.

2.2 Electrochemistry

Cyclic voltammetry experiments were carried out in CH_3CN under N_2 with 0.1 M tetrabutylammonium hexafluorophosphate ($TBAPF_6$) as supporting electrolyte and glassy carbon as working electrode. Bulk electrolysis experiments were performed at −1.5 V and −1.63 V *vs.* Fc^+/Fc on a mercury-pool electrode in 8 mL CH_3CN, in the presence of TFA (100 mM), the complexes (1 mM) and tetrabutylammonium hexafluorophosphate, $TBAPF_6$ (0.1 M). Foot-of-the-wave analysis (FOWA) was performed to gain information concerning the rate constants (k_1, k_2) relative to the proton transfer step of the catalytic process.[34–36] The rate constants were extrapolated as average at various concentrations of acid (TFA solutions in the range 5–20 mM) and scan rates (0.7–47 V s^{-1}). Further details of the calculations are shown in the ESI (Sections S4 and S5).

2.3 Photochemistry

Photoinduced hydrogen production experiments were performed in fully aqueous solutions with 1 M acetate buffer (pH =

4) in the presence of [Ru(bpy)$_3$]Cl$_2$ (0.5 mM) as photosensitizer, and ascorbic acid (0.1 M) as proton source and catalyst (5 μM). The solutions were irradiated with a blue light at 475 nm and 20 °C for 6 h. These conditions were selected according to the best conditions previously found for **C1**.[26,27] Turnover numbers (TONs), turnover frequencies (TOFs) and quantum yields (QYs) were calculated according to the procedures previously reported by us.[30]

Nanosecond transient absorption measurements were performed with a custom laser spectrometer consisting of a Continuum Surelite II Nd:YAG laser (FWHM = 8 ns) with a frequency doubling (532 nm, 330 mJ) option, an Applied Photophysics Xe light source including a mod. 720 150 W lamp housing, a mod. 620 power-controlled lamp supply and a mod. 03-102 arc lamp pulser. Laser excitation was provided at 90° with respect to the white light probe beam. Light transmitted by the sample was focused onto the entrance slit of a 300 mm focal length Acton SpectraPro 2300i triple grating, flat field, double exit monochromator equipped with a photomultiplier detector (Hamamatsu R3896). Signals from the photomultiplier (kinetic traces) were processed by means of a TeledyneLeCroy 604Zi (400 MHz, 20 GS s^{-1}) digital oscilloscope. Before all the measurements the solutions were purged with nitrogen for 10 minutes.

2.4 Computational setup

Theoretical investigations were performed only for **C2** and **C3**, since the two tautomeric forms of **C4** impeded a straightforward comparison between the experimental and calculated properties. The general computational strategy used here for the calculation of the oxidation potentials, reaction intermediates and energy barriers is the same as that employed in our previously published studies on heptacoordinate cobalt complexes (including **C1**).[26,27,30] Redox potentials in acetonitrile were calculated as free energy differences in solution. The Gibbs free energy in solution of a species i ($G^{\mathrm{i}}_{\mathrm{solv}}$) is defined as $G^{\mathrm{i}}_{\mathrm{solv}} = G^{\mathrm{i}}_{\mathrm{vac}} + \Delta G^{\mathrm{i}}_{\mathrm{solv}}$, where $G^{\mathrm{i}}_{\mathrm{vac}}$ is the Gibbs free energy in the gas phase (the gas phase energy with zero-point energy and thermal corrections) and $\Delta G^{\mathrm{i}}_{\mathrm{solv}}$ is the free energy of solvation. $G^{\mathrm{i}}_{\mathrm{vac}}$ is obtained by performing a single point calculation at the optimized geometry *in vacuo*, followed by frequency calculations in order to include the vibrational contribution to the total partition function. The solvation free energy, $\Delta G^{\mathrm{i}}_{\mathrm{solv}}$, was obtained by a single-point calculation in solution and a reference calculation in the gas phase at the geometry optimized in solution. The absolute potentials calculated *vs.* vacuum were converted to potentials *vs.* Fc$^+$/Fc by adding −4.80 V as reported in ref. 44. In line with our previous studies and following the procedure reported in ref. 37 to calculate the relative free energies for the considered reaction steps, we used values of $G^*(\mathrm{H^+}_{(\mathrm{s})}) = -266.5$ kcal mol^{-1},[38] $G^0(\mathrm{e^-}_{(\mathrm{g})}) = -0.868$ kcal mol^{-1} (ref. 39) and $G^0(\mathrm{H}_{2(\mathrm{g})}) = -739.5$ kcal mol^{-1}. A value of −4.44 eV was used for the *vacuum* level with respect to the Normal Hydrogen Electrode (NHE) in acetonitrile.[37] Preliminary benchmark calculations on the redox potentials of the systems considered here showed, however, that the best agreement with experiments was obtained when using the PBE0 functional (25% of Hartree–Fock exchange), instead of B3LYP, that was adopted in our previous studies.[40] Therefore, we performed all the DFT calculations to determine energy minima, transition states and relaxed scans for the different reduction and oxidation steps, by using the PBE0 exchange and correlation functional and the 6-311G* basis set. The solvent (acetonitrile) was taken into account in all cases by the implicit IEF (Integral Equation Formalism) method of the PCM (Polarizable Continuum Model).[41] For a proper comparison of **C2** with the experimental values, two different mechanisms were considered: (i) initial protonation by the medium, before starting the H$_2$ evolution process by accepting 2 electrons and 2 protons (*i.e.*, 2E2H) or (ii) final protonation by an explicit acidic medium after reaching the second protonation step. In the latter case, a CH$_3$COOH molecule (weak acid), a CF$_3$COOH molecule (TFA, strong acid), and a protonated water cluster of 3 water molecules (*i.e.*, $2\mathrm{H_2O}\cdots\mathrm{H_3O^+}$) were explicitly included in the calculations (see Fig. ES25 in the ESI†).

For **C2** and **C3** the stability of the high and low spin configurations was preliminarily verified by single point electronic structure calculations in implicit acetonitrile solvent, using DFT (PBE0 functional) and MP2 methods with the 6-311G* basis set (Table ES5 in the ESI†).

All calculations were performed with the Gaussian16 package,[42] including the thermochemical characterization of each stationary point on the potential energy surface (minima and transition states) through frequency calculations, thus obtaining enthalpy and Gibbs free energy.

3. Results and discussion

3.1 Synthesis and characterization

The ligands **L2**, **L3** and **L4** (Fig. 1) were synthesised from the reaction of *N*,*N*-bis-(6-(2,2′-bipyridyl)methyl)amine with the pyridine bearing various substituent groups in the presence of the base *N*,*N*-diisopropylethylamine. The synthesis of **L1** was previously described.[26] The reaction of the ligands **L2**, **L3** and **L4** with Co(BF$_4$)$_2$·6H$_2$O or CoSO$_4$·7H$_2$O in methanol led to the formation of the complexes (*i.e.* **C2**: [Co(II)**L2**](BF$_4$), **C3**: [Co(II)**L3**](BF$_4$)$_2$, **C4**: [Co(II)**L4**](BF$_4$)$_2$ with BF$_4^-$ and **C3′**: [Co(II)**L3**]SO$_4$ and **C4′**: [Co(II)**L4**]SO$_4$ with SO$_4^{2-}$ as counterions, respectively) which were precipitated and washed with diethyl ether. **C3″**: [Co(II)**L3**](PF$_6$)$_2$ (counterion = PF$_6^-$) was synthesized by adding NH$_4$PF$_6$ to a solution of **C3′** (counterion = SO$_4^{2-}$) in water.

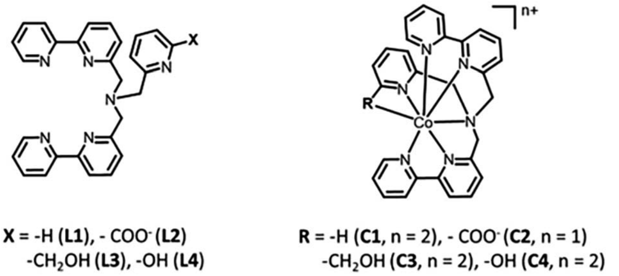

Fig. 1 Structures of the ligands L1–L4 (left) and the corresponding Co complexes (C1–C4). For the sake of clarity, the description of the different counterions of the complexes is provided in the text.

Further details of the synthesis and the characterization of the compounds are shown in the ESI (Section S2). The structural study conducted on single crystals with X-ray diffraction (Fig. 2) reveals that complexes **C2** and **C3″** possess a heptacoordinate geometry which can be described as a face capped octahedron, similarly to the archetypical complex **C1**.[26] The metal centre in **C2** and **C3″** is coordinated to six N and to the O of the substituents on the pyridine. The coordination bonds lengths are in the range of 2.11–2.41 Å, *i.e.* very close to the bond length range observed in **C1** (2.09–2.41 Å). The longest bond in both the complexes is Co–N1 (with a length of 2.4101(13) Å and 2.3080(17) Å for **C2** and **C3″**, respectively). The angles closest to linearity are N2–Co–N5 for **C2** (*ca.* 158°) and N4–Co–N3 (*ca.* 161°) for **C3”**. In the case of complexes derived from **L4**, two different tautomeric structures at the pyridine level were observed, namely **C4** (enol form) and **C4′** (keto form). In both structures the metal centre shows a hexacoordinate geometry: in **C4′** it coordinates the oxygen of the sulphate counterion (Co–O bond distance = 2.0102(14) Å), whilst in **C4** it coordinates all six N of the ligand. However, in spite of the different geometry, **C4** and **C4′** have structural parameters and geometries similar to **C2** and **C3″** with bond distances in the range of 2.01–2.34 Å and the angle close to linearity N2–Co–N5 (*ca.* 156° and *ca.* 160° for **C4** and **C4′**, respectively). The ^{1}H-NMR spectra of the complexes in D_2O confirmed the paramagnetic nature of Co(ii). Values of magnetic efficiency (μ_{eff}) = 3.9, 4.1 and 3.8 BM were calculated for **C2**, **C3** and **C4** respectively, corresponding to high spin configurations with three unpaired electrons (Fig. ES1†).[26,43] Indeed, electronic structure calculations also predict the high spin configuration to be the most stable one for both **C2** and **C3** (Table ES5 in the ESI†), thus corroborating the reliability of the DFT protocol. Ultraviolet-Visible (UV-Vis) absorption spectra were recorded in CH_3CN in the presence and in the absence of trifluoroacetic acid (TFA), to evaluate the possibility of protonating the complexes (Fig. 3). The final volume of the solutions (2 mL) was kept constant to minimize the dilution effect on the absorption spectra. **C2** shows a broad signal around 486 nm and a less intense peak at 634 nm. In the presence of 1 to 20 equivalents of TFA, the high energy band assumes a more defined shape and it is slightly red-shifted (489 nm), while the peak at 634 nm disappears. Only a slight hypsochromic shift is observed in the presence of acid in the UV-Vis spectra of **C3**, characterized by a shoulder at 490 nm. **C4** displays a broad absorption at 460 nm, a slightly less intense peak at 511 nm and a weak peak at 676 nm. Upon addition of the acid, the first peak is shifted to 456 nm, the second peak remains at the same position but with a slightly higher intensity with respect to the first peak and the peak at 676 nm disappears. As expected, the absorption spectrum of complex **C1** (Fig. 3a) does not show any modification upon addition of acid.

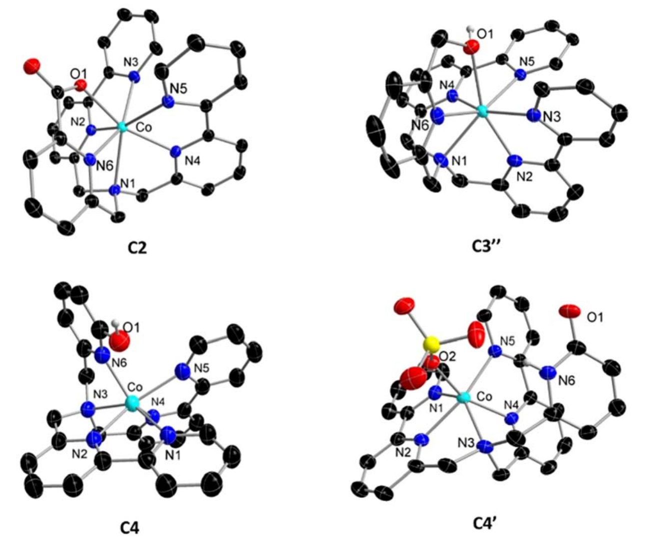

C2 C3″ C4 C4′

Fig. 2 Crystal structures of complexes **C2**, **C3″** and the two tautomers **C4** (enol form) and **C4′** (keto form). Colour code: Co (turquoise), N (blue), O (red), C (black), S (yellow), H (white). Non-coordinating counterions (*i.e.*, BF_4^-, PF_6^- and SO_4^{2-}), solvents, and other hydrogen atoms have been omitted for clarity.

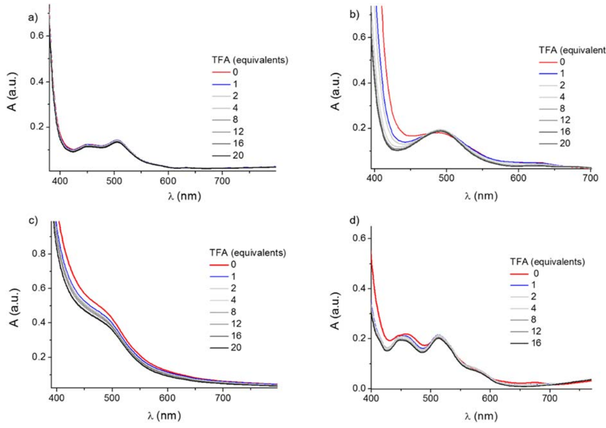

Fig. 3 UV-Vis spectra of 4 mM solutions of complexes **C1** (a), **C2** (b), **C3** (c), and **C4** (d) in CH_3CN at increasing amounts of TFA keeping the final volume (2 mL) unchanged.

3.2 Electrochemical studies

The cyclic voltammograms (CV) of each complex (Fig. 4) display two reversible and diffusion-controlled waves (Fig. ES2–ES4†). The first electrochemical waves at −1.88 V for **C2**, −1.64 V for **C3** and −1.70 V for **C4**, as well as the second redox systems at −2.13 V for **C2**, −2.03 V for **C3** and −2.14 V for **C4** (all values *vs.* Fc^+/Fc, Table 1) can be preferentially attributed, by DFT calculations, to bipyridine ligand-centred reduction, with substantial involvement of the metal $Co^{II/I}$ reduction for the first wave (Fig. ES20†). The calculated absolute potentials for the first/second reduction obtained *vs.* vacuum and converted to potentials *vs.* Fc^+/Fc[44] (Table ES6†) are −2.03/−2.18 and −1.80/−2.09 V for **C2** and **C3**, respectively, in overall good agreement with the experimental values. The first signals of **C2**, **C3** and **C4** show a peak-to-peak separation of around 66 mV in accordance with the theoretical value of 59 mV for a monoelectronic Nernstian process, while the second waves have a peak-to-peak separation of 110 mV for **C3** and **C4** and 50 mV for **C2** (Fig. ES2–

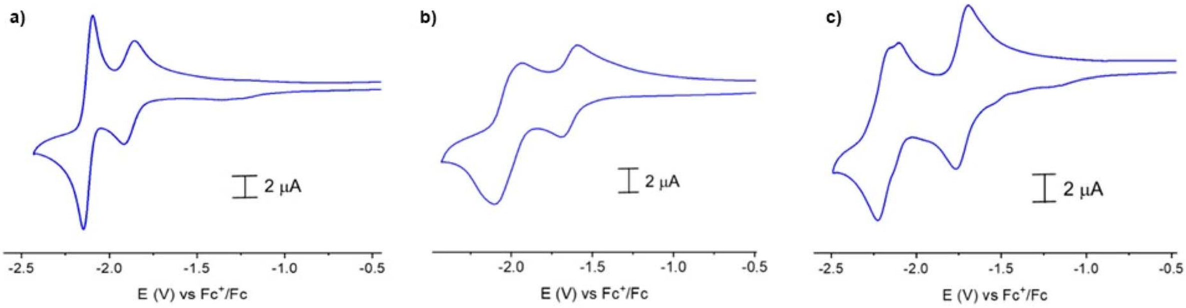

Fig. 4 Cyclic voltammograms (CVs) of 1 mM solutions of complexes (a: **C2**, b: **C3**, c: **C4**) recorded at 0.1 V s^{-1} in CH_3CN with 0.1 M $TBAPF_6$, with glassy carbon as working electrode.

Table 1 Reduction potentials ($E_{1/2}$) in acetonitrile, half-wave potentials of the catalytic waves (E_{cat}) and difference between E_{cat} and Co$^{II/I}$ for **C1**, **C2**, **C3**, and **C4** with TFA

	First reduction (V *vs.* Fc$^+$/Fc)	Second reduction (V *vs.* Fc$^+$/Fc)	E_{cat} (V *vs.* Fc$^+$/Fc)	$E_{cat} - E_{CoII/CoI}$ (mV)
C1 (ref. 27)	−1.50	−2.06	−1.41	39
C2	−1.88	−2.13	−1.58	300
C3	−1.64	−2.03	−1.57	70
C4	−1.70	−2.14	−1.46	240

ES4†). As expected, the functionalization of the ligand influences the electronic properties of the complex. In fact, the first redox signal of **C2**, **C3** and **C4** appears at potentials more negative than for the unsubstituted complex **C1** (with the first reduction at −1.50 V *vs.* Fc$^+$/Fc).

The second reduction of **C2** and **C4** also occurs at potentials more negative than those of **C1** (*i.e.*, the second reduction at −2.06 V *vs.* Fc$^+$/Fc), whilst **C3** displays the second reduction at potentials close to those of **C1**. However, the smaller difference (<0.1 V) between the redox potentials of the second wave with respect to those of the first wave (>0.2 V) supports a minor effect of the substituted pyridine on the ligand-based redox event, as expected on the basis of the preferential involvement of the bipyridyl moieties in the second reduction. As a final remark, while two neat redox processes can be observed for complexes **C2** and **C3**, additional minor features can be discerned in the case of **C4** (Fig. 4c) which can be associated with the coming into play of ligand tautomerism, possibly induced by trace amounts of water in the acetonitrile solvent. As a matter of fact, although the 2-pyridone tautomer is expected to be the most stable species in solution for the free ligand,[45] coordination to the cobalt centre should favour the hydroxypyridine form thus leading to a hexacoordinated species in solution. The similar redox potentials and CV shape observed for **C4** and the remaining complexes **C1–3** strongly support this latter hypothesis, with any changes in the tautomeric equilibrium possibly imparted by the occurrence of hydrogen bonding interactions in the presence of water (or trace amounts thereof) or acid sources (see below).

For all the complexes, the addition of increasing amounts of TFA as proton source triggers the appearance of catalytic waves at potentials more positive than those of the Co$^{II/I}$ standard reduction potentials (Fig. 5 and ES5–ES7 of the ESI†). The half-wave potentials of the catalytic waves (*i.e.*, E_{cat}) are shifted

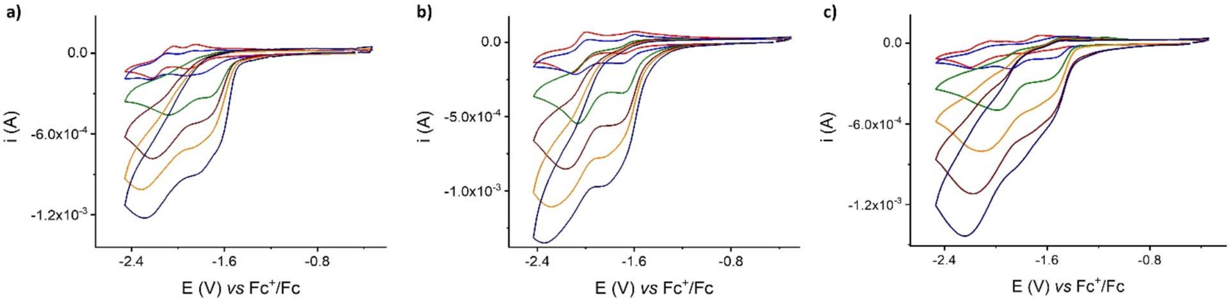

Fig. 5 Cyclic voltammograms of 1 mM of catalysts **C2** (a), **C3** (b) and **C4** (c) recorded in CH_3CN with 0.1 M $TBAPF_6$ at 30 V s^{-1} with glassy carbon as working electrode and increasing amounts of TFA (0 red, 1 blue, 5 green, 10 brown, 15 orange and 20 navy blue mM).

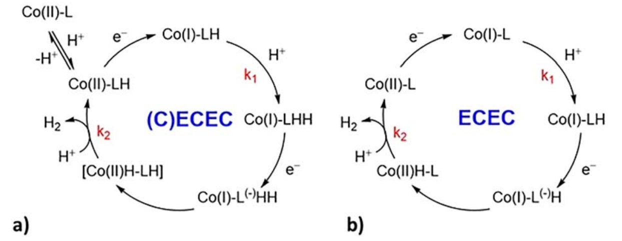

Scheme 1 Proposed pathways for H_2 evolution under electrochemical conditions in acetonitrile solution with TFA as the proton source: (a) (C)ECEC for complexes **C2** and **C4**; (b) ECEC mechanism for complexes **C3** and **C1**.[27]

towards more positive potentials with respect to $Co^{II/I}$. In particular, a big shift of *ca.* 300 mV is observed with **C2** and **C4** and a less pronounced shift of 70 mV is observed with **C3** (Table 1). E_{cat} is independent of scan rates and acid concentrations as shown in Fig. ES12.† The considerable shifts of E_{cat} for **C2** and **C4** (300 and 240 mV, respectively) together with the appreciable variation of the UV-Vis spectra in the presence of TFA (Fig. 3) suggest that a protonation of the catalyst takes place prior to the first electron transfer of the catalytic cycle (Scheme 1a). **C2** protonation is expected to involve the carboxylate group of the ligand, while in the case of **C4** the acid source most likely shifts the tautomeric equilibrium of the hydroxypyridine towards the 2-pyridone form leading to decoordination and protonation. Conversely, in the case of **C3**, the absence of major spectral changes in the UV-Vis spectra in the presence of TFA together with the small shift in potential strongly supports a catalytic mechanism similar to the one established for the prototype complex **C1** (Scheme 1b).[27]

Bulk electrolysis experiments confirmed the production of molecular hydrogen in proximity of the catalytic wave (Table ES1 and Fig. ES8†). In particular, at −1.50 V *vs.* Fc^+/Fc **C2**, **C3** and **C4** gave faradaic yields of 51%, 73% and 53% respectively, while at −1.63 V *vs.* Fc^+/Fc faradaic yields of 92% for **C2** and 85% for **C3** and **C4** were achieved.

The general mechanism proposed for **C3** belongs to the ECEC category (with E being the electron transfer and C the chemical, *i.e.* protonation, step, Scheme 1b) with the second electron transfer easier than the first and the second protonation slower than the first.[46] Foot-of-the-wave analysis (FOWA) was thus used to determine the rate constant of the first protonation step leading to a value of $k_1 = 3.1\ (\pm 0.8) \times 10^7\ M^{-1}\ s^{-1}$. Then, following the same procedure used for **C1** in our previous work,[27] from the potential shift of the catalytic wave with respect to the Co(II)/Co(I) redox couple the rate constant of the second protonation step was attained, $k_2 = 1.6\ (\pm 0.5) \times 10^5\ M^{-1}\ s^{-1}$. In the case of **C2** and **C4** this approach cannot be applied because of the significant shift of the catalytic wave with respect to the Co(II)/Co(I) reduction. This observation, together with the changes of the absorption spectra in the presence of acid, is consistent with a protonation of the catalyst taking place before the catalysis (Scheme 1a). This process produces a Co(II)LH species which is the starting point of the catalytic hydrogen evolution reaction, most likely following a (C)ECEC mechanism.[47] However, the reduction potential of the Co(II)LH species is unknown, thus FOWA cannot be applied to extract kinetic information. A recently published method shows that catalytic potential measured at high scan rates (at which the catalysis is likely outrun) can actually provide the redox potential of the Co(II)LH/Co(I)LH species.[47] Unfortunately, in the case of **C2** substantial catalysis can still be observed up to 47 V s^{-1} in the presence of 15 eq. of acid (Fig. ES5†). Therefore, in the case of **C2** and **C4** the plateau currents extracted under scan rate independent conditions (Fig. ES11†) were used, giving catalytic rate constants as high as $1.1\ (\pm 0.2) \times 10^5\ M^{-1}\ s^{-1}$ and $3.4\ (\pm 0.6) \times 10^4\ M^{-1}\ s^{-1}$ for **C2** and **C4**, respectively. Assuming that even for these complexes the second protonation is the rate-determining step of the catalysis, as observed for **C1** and **C3**, these rate constants thus correspond to k_2 values. Further discussion on the kinetic analysis (including relevant equations and plots) is provided in the ESI (Section S5). Interestingly, in the case of **C2** and **C4**, the use of acetic acid as the proton donor triggers the appearance of catalytic waves with E_{cat} near the $Co^{II/I}$ couple (Fig. ES13†). These results suggest that protonation of the pristine form of the catalyst does not occur with a weaker proton source and hence the HER catalysis follows a typical ECEC mechanism (Scheme 1b). The failure to achieve protonation of the complexes under weakly acidic conditions, however, translates in the HER by **C2** and **C4** being promoted at more negative potentials than with TFA. This evidence is particularly relevant towards the application of **C2** under photochemical conditions (see below) since a highly negative reduction potential is associated with the Co(II)/Co(I) step.

Finally, from the values of k_1 and k_2 attained for complexes **C2–4** in acetonitrile using TFA as proton source, a TOF_{max} (turnover frequency maximum) of $1.1 \times 10^5\ s^{-1}$, $1.6 \times 10^5\ s^{-1}$ and $0.34 \times 10^5\ s^{-1}$ for **C2**, **C3** and **C4** respectively can be extrapolated for a 1 M acid solution, *i.e.*, the standard conditions proposed for a rational benchmark of the performances of H_2 evolution, to obtain the catalytic Tafel plot (Fig. 6). Such a plot can be traced for each catalyst knowing TOF_{max}, E_{cat} and the apparent equilibrium potential of the H^+/H_2 couple (0.61 V *vs.* $Fc^{+/}Fc$).[19,35,48] As shown in Fig. 6, the catalytic Tafel plots of the catalysts are comparable. In particular, a significant

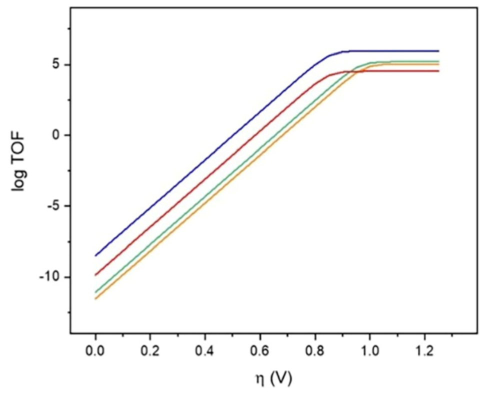

Fig. 6 Catalytic Tafel plots relating TOFs and applied overpotentials (η) for **C1** (blue), **C2** (orange), **C3** (green), and **C4** (red).

catalytic activity (*i.e.*, log(TOF) > 1) is reached at overpotentials larger than 500 mV in the case of **C1**. On the other hand, the other catalysts of the series require higher overpotentials to reach a catalytic activity: 600 mV in the case of **C4** and 700 mV in the case of **C2** and **C3**.

3.3 Photochemical studies

Light-driven hydrogen production was studied upon irradiation of 5 μM solutions of each catalyst in 1.0 M acetate buffer (pH = 4) in the presence of 0.1 M ascorbic acid and 0.5 mM $[Ru(bpy)_3]^{2+}$ (bpy = 2,2′-bipyridine) as sacrificial electron donor and photosensitizer, respectively. In this three-component system hydrogen evolution is expected to occur *via* a reductive route involving excitation of the $[Ru(bpy)_3]^{2+}$, reductive quenching by the ascorbate donor, and subsequent electron transfer from the reduced sensitizer to the catalyst (HEC) either in its pristine or one-electron reduced form (eqn (1)–(3)).[23]

$$[Ru(bpy)_3]^{2+} + h\nu \rightarrow {}^*[Ru(bpy)_3]^{2+} \tag{1}$$

$$^*[Ru(bpy)_3]^{2+} + Asc^- \rightarrow [Ru(bpy)_3]^+ + Asc^{\bullet} \tag{2}$$

$$[Ru(bpy)_3]^+ + HEC_{ox} \rightarrow [Ru(bpy)_3]^{2+} + HEC_{red} \tag{3}$$

Fig. 7a shows the evolution of H_2 during the catalysis for **C3**, **C4** and **C1** (herein used as a reference), while Fig. 7b reports the maximum turnover numbers with respect to the moles of catalysts used (TONs) and turnover frequencies (TOFs, *i.e.*, moles of H_2 per mole of catalyst per min). The catalytic trace of **C2** is not reported since negligible hydrogen evolution was observed under the present experimental conditions. Inspection of the kinetic data shows that complex **C4** reached a TON of 626 with a maximum TOF of 12.5 min^{-1}, whilst **C3** reached a TON of 1333 with a maximum TOF of 11.0 min^{-1}, which is slightly higher than that of **C1** under the same conditions (TON of 1166 and TOF of 7.5 min^{-1}). The estimated quantum yields were 4.9%, 7.2%, and 8.2% for **C1**, **C3** and **C4**, respectively. The formation of nanoparticles as decomposition products of **C3** and **C4** was ruled out by mercury poisoning experiments, *i.e.*, by running the photochemical experiments in the presence of 1 mL of mercury and under the same catalytic conditions reported above. Under these conditions no appreciable variation of the photocatalytic behaviour was indeed observed, as shown in Fig. ES14.†

Transient absorption spectroscopy was then employed to conduct a kinetic characterization of the photoinduced events. Upon excitation at 532 nm of a solution containing 70 μM $[Ru(bpy)_3]^{2+}$, 0.1 M ascorbic acid, and 0.1 mM **C3** in 1 M acetate buffer, a transient spectrum develops within a μs that features an absorption at 510 nm (prompt spectrum in Fig. 8a). This spectrum can be assigned to the reduced sensitizer $[Ru(bpy)_3]^+$ formed *via* reductive quenching of the triplet excited state of the $[Ru(bpy)_3]^{2+}$ chromophore by the ascorbate sacrificial donor (eqn

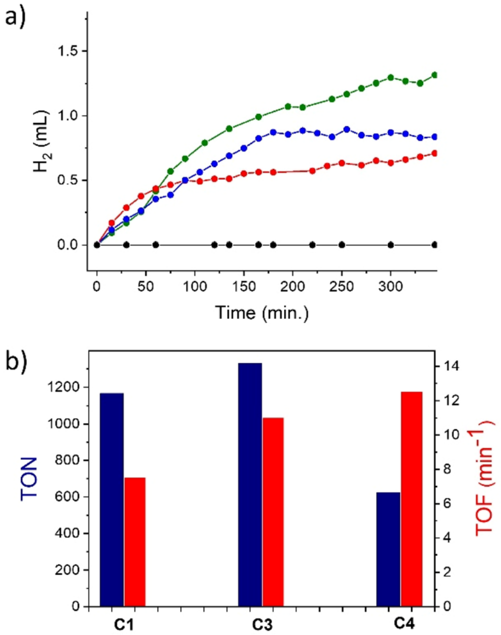

Fig. 7 (a) H_2 evolution in mL over time for solutions of 5 μM catalysts **C1** (blue), **C3** (green), and **C4** (red) and without catalysts (black). The experiments were performed in 1.0 M acetate buffer at pH 4.0 with 0.1 M ascorbic acid and 0.5 mM $[Ru(bpy)_3]Cl_2$ at 20 °C and the solutions were irradiated with LED light at 475 nm. (b) Maximum TONs and TOFs for **C1**, **C3** and **C4**.

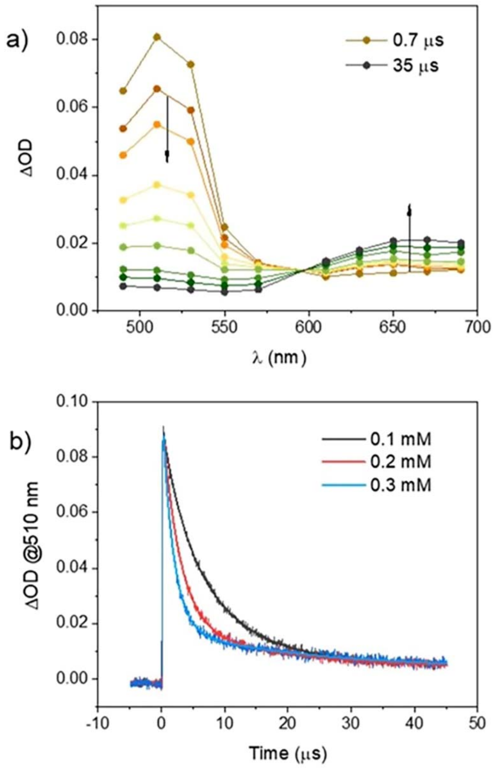

Fig. 8 (a) Transient absorption spectra between 0.7 and 35 μs obtained by laser flash photolysis (excitation at 532 nm) of a solution containing 70 μM $[Ru(bpy)_3]^{2+}$, 0.1 M ascorbic acid, and 0.1 mM **C3** in 1 M acetate buffer; (b) kinetic traces at 510 nm at 0.1–0.3 mM **C3** (fitting was performed using a biexponential function in which the first component is associated with the reaction in eqn (3), and the second component with the charge recombination between Co(I) and the ascorbate radical).

(1) and (2)).[49,50] The subsequent spectral evolution (Fig. 8a) is characterized by the decrease of the 510 nm absorption and the concomitant formation of a new band at $\lambda > 600$ nm. This spectral evolution is accompanied by a clear isosbestic point at 595 nm, which can be attributed to the reduction of the cobalt complex **C3** by photogenerated $[Ru(bpy)_3]^+$ (eqn (3)). The broad absorptions in the visible spectrum are indeed characteristic spectral features of Co(I) species of polypyridine complexes,[27,50–54] as further confirmed by spectroelectrochemical analysis (Fig. ES15†). Similar spectral changes are monitored using complex **C4** under identical experimental conditions (Fig. ES16†).

Interestingly, the kinetics of the decay at 510 nm is observed to be dependent on the concentration of the cobalt complex (see Fig. 8b for **C3** and Fig. ES16† for **C4**), as expected based upon the bimolecular nature of the electron transfer reaction in eqn (3). Under pseudo-first order kinetic conditions, fitting of the kinetic traces and subsequent normalization by the catalyst concentration (Fig. ES16 and ES17 of the ESI†) allows the determination of the bimolecular rate constant for the electron transfer process from the photogenerated $[Ru(bpy)_3]^+$ to the cobalt complex (eqn (3)). These estimates yield values of 1.6×10^9 M^{-1} s^{-1} and 1.9×10^9 M^{-1} s^{-1} for **C3** and **C4**, respectively, close to the diffusion-controlled kinetic regime and comparable to those experimentally determined for the parent compound **C1** (2.2×10^9 M^{-1} s^{-1}) and related substituted analogues.[27,30] The transient absorption spectrum associated with the Co(I) species finally decays to the baseline within a few hundred μs with a clear second-order kinetics (Fig. ES18 and ES19† for **C3** and **C4**, respectively) due to charge recombination with the oxidized ascorbate.[27,52] Overall, the transient absorption spectroscopic investigation establishes that: (i) similar to most polypyridine cobalt complexes both catalysts **C3** and **C4** rapidly react with photogenerated $[Ru(bpy)_3]^+$ thus accounting for the intrinsic high catalytic activity of this class of compounds within the aforementioned photochemical reaction scheme;[23] (ii) the product of such an electron transfer event is a Co(I) catalyst species as monitored from the peculiar spectral fingerprints, (iii) the failure to observe additional spectral features upon Co(I) decay, beside those associated with charge recombination with the ascorbate radical, suggests that protonation of the one-electron reduced catalyst, likely involving a detached pyridine as supported by DFT calculations (see below), does not occur in a concerted fashion and is thus slower than experimentally detectable; (iv) the similar electron transfer kinetics observed for **C1**, **C3**, and **C4** possibly indicate that any differences in terms of catalysis rates and efficiencies within the series are mainly ascribable to the kinetics of either protonation or hydrogen release. In this respect, the improved activity of complex **C3** with respect to the remaining complexes of the series is well consistent with the highest catalysis rate measured in electrocatalytic experiments. On the other hand, the performance of **C4** apparently contrasts with the slowest catalysis rate measured under electrochemical conditions. This can be in part attributed to possible effects exerted by the different solvent environments (acetonitrile in the electrochemical experiments *vs.* water in the photochemical ones) which might impact to some extent on the speciation of the catalyst, according to the observed ligand tautomerism. As to the failure to observe any activity by complex **C2**, this can be associated with inefficient protonation of the pristine complex in the aqueous buffer under weakly acidic conditions. Under this assumption, one-electron reduction of complex **C2** (−1.88 V *vs.* Fc$^+$/Fc, Table 1) by the photogenerated $[Ru(bpy)_3]^+$ ($E = -1.28$ V *vs.* NHE in water,[55] corresponding to −1.81 V *vs.* Fc$^+$/Fc[56]) is indeed expected to be endergonic.

We would like to stress, however, that direct comparison between performance-related parameters in electrochemical and light-driven catalysis is usually too speculative and should be taken with caution since different kinetic limiting steps may actually determine the overall activity of the catalysts in either experiment. Interestingly, different rate-determining steps were recently observed by Llobet and co-workers in electrochemical and photochemical experiments when investigating the hydrogen evolution reaction of cobalt tetraazamacrocycles.[57]

3.4 Computational analysis

Quantum mechanical calculations were performed on complexes **C2** and **C3** to corroborate the hypothesis of the different proposed mechanisms. In fact, the presence of two tautomeric forms in **C4** impeded a straightforward comparison between the experimental and calculated properties.

Our previous mechanistic studies on **C1** and on other related derivatives clearly pointed to an ECEC catalytic mechanism.[27,30] In more detail, based on DFT/TDDFT results and transient absorption spectroscopy measurements, we proposed that, after a first reduction of the metal centre giving a Co(I) intermediate, a protonation of the bipyridyl and/or pyridyl moieties takes place. In fact, in this family of compounds the direct protonation of the metal centre to give Co(III)–H is thermodynamically unfavourable. These first two steps are then followed by a second reduction and protonation event to form H_2 (Scheme 1b). Here, experimental evidence suggests that complexes **C2** and **C3** both follow an ECEC mechanism, analogously to **C1**, although **C2** needs to be initially protonated, thus formally resulting in a (C)ECEC mechanism.

In more detail, for complex **C2**, both UV-Vis absorption spectroscopy (Fig. 3) and the electrochemical potential shift (Fig. 4 and 5) suggest the steady formation of a protonated complex. Consistently, the computational investigation confirms that a Co(II)**-OfH** (*i.e.* the complex protonated on the non-coordinated oxygen of the carboxylic group, the adopted nomenclature is shown in Fig. ES22†) species is formed spontaneously by proton transfer from the surrounding media. Interestingly, this species preserves the stable 7-fold coordination geometry of the metal centre. The first step is expected to involve a **Co(II)-OfH** + e$^-$ → **Co(I)-OfH** reduction (see the left panel of Fig. 9). Energy shift values are given in Table ES6.† Subsequent protonation and reduction of the **Co(I)-OfH** species then leads to the generation of three near-in-energy intermediates involving a doubly protonated ligand, namely **Co(I)-PY$^{(-)}$H-OfH**, **Co(I)-BPY1$^{(-)}$H-OfH**, and **Co(I)-BPY2$^{(-)}$H-OfH**. For the last protonation triggering hydrogen elimination, two different pathways were considered: (i) intermolecular proton transfer from the pyridyl/bipyridyl moiety to the

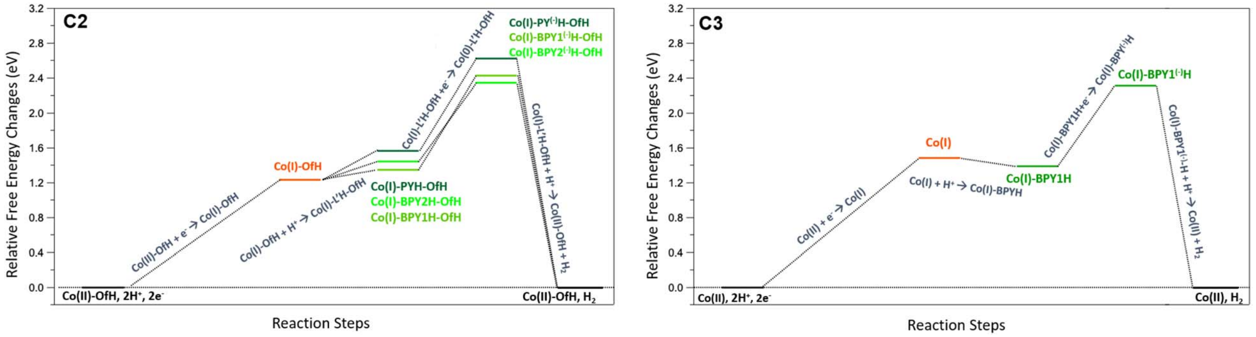

Fig. 9 Calculated free energy profiles in acetonitrile for the possible reaction steps involved in the proposed mechanism for **C2** (left) and **C3** (right). Values and profiles of the relative free energy changes (Δ*G*) are given in Table ES6.† The zero is defined as the free energy of the Co(II) compound (**Co(II)-OfH** for **C2**; Co(II) for **C3**) plus that of two protons with an activity of 1 (apparent pH = 0 in acetonitrile) and two electrons at the potential of the NHE in acetonitrile. For **C2** L′ = BPY1, BPY2, and PY. The corresponding structures can be found in Fig. ES26.†

cobalt centre, prior to re-protonation of the ligand and (ii) bimolecular protonation of the cobalt centre followed by hydrogen formation. The former mechanism is not feasible for the two intermediates involving the protonated pyridyl moiety (**Co(I)-PY$^{(-)}$H-OfH**, activation energy barrier of 22.09 kcal mol^{-1} and free energy difference of 13.08 kcal mol^{-1}) and those involving the bipyridyl moieties (**Co(I)-BPY1$^{(-)}$H-OfH** and **Co(I)-BPY2$^{(-)}$H-OfH**). Conversely, bimolecular protonation of the cobalt centre according to mechanism (ii) results in the face-to-face arrangement of two hydrogen atoms, favouring the generation of molecular hydrogen (see especially the **Co(II)H-PYH-OfH** structure in Fig. ES26,† as well as its energy profile, together with **Co(II)H-BPY1H-OfH** and **Co(II)H-BPY2H-OfH**, in Fig. 10, left). Interestingly, this process is particularly feasible for **Co(II)H-PYH-OfH** (Fig. 10, left), being almost barrierless (+0.05 eV, +1.11 kcal mol^{-1}) and slightly exergonic (−0.16 eV, −3.61 kcal mol^{-1}). This mechanistic scenario is further confirmed by theoretical analysis of the possible, alternative CEEC mechanism (Fig. ES21†). As a matter of fact, for this latter, highly endergonic pathways (by +3.18 eV and +3.34 eV) are envisioned after the first protonation towards the formation of the **Co(I)-Of$^{(-)}$H** intermediate upon two electron transfer processes. At this stage hydrogen elimination is thermodynamically hampered, whilst H_2 production becomes feasible only when a strong acid such as TFA is hydrogen-bonded to the pyridyl-COOH moiety or in the presence of an acidic $(H_2O)_2(H_3O^+)$ cluster (Fig. ES25†). Indeed, since the hydrogen atom of the pyridyl-COOH group is required to form H_2, the acidic medium is necessary to mediate, in a concerted fashion, H_2 formation and –COOH regeneration. This computational evidence thus supports the proposed (C)ECEC mechanism. Concerning complex **C3**, experimental evidence suggests a typical ECEC mechanism as observed for **C1**. The corresponding mechanistic analysis is reported in Fig. 9 (right) with energy shift values reported in Table ES6.† After the first reduction step, **Co(II)** + e$^-$ → **Co(I)**, involving de-coordination of the CH_2OH group, the most favourable thermodynamic pathway goes through the formation of a **Co(I)-BPY1H** intermediate upon protonation (−0.10 eV, −2.3 kcal mol^{-1}). This latter is stabilized by an intramolecular N–H⋯OH bond between the protonated **BPY1H** moiety and the OH group of the pyridyl moiety. On the other hand, protonation of the other available bipyridyl to generate **Co(I)-BPY2H** as the first protonation step is predicted to be more than 1.08 eV (25 kcal mol^{-1}) higher in energy, due to the impossibility of forming any hydrogen bond. The second reduction step then involves the formation of a **Co(I)-BPY1$^{(-)}$H** intermediate. Finally, to complete the ECEC mechanism the last chemical step implies protonation of the cobalt centre, thus forming a **Co(II)H-BPY1H**

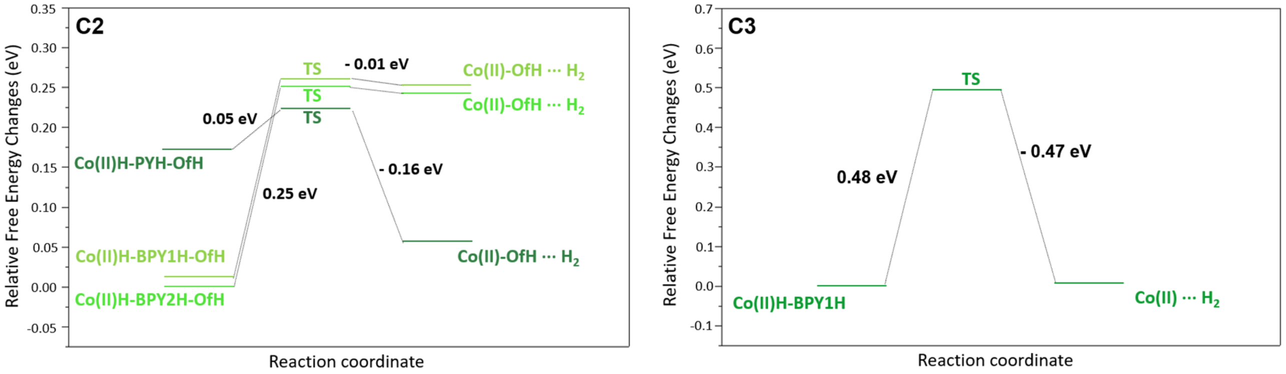

Fig. 10 Calculated free energy profiles (Δ*G*) starting from the second protonation step until formation of H_2, for **C2** (left) and **C3** (right). At this step, once formed, H_2 is still in interaction with the complex (see structures in Fig. ES26†). The structures corresponding to stationary points (minima and transition states, TS) are given in Fig. ES26,† including the imaginary frequency of the most relevant TSs.

intermediate that further evolves to produce H_2 similarly to what is observed for the parent **C1**.[27] As depicted in Fig. 10 (right) and Fig. ES26† hydrogen elimination from the **Co(II)H-BPY1H** species occurs thanks to the close interaction between the H atom of the protonated bipyridine moiety (H_a) and the H atom (H_b) of the protonated Co centre (NH_a-BPY···H_b-Co distance of 1.80 Å). For this reaction a transition state of *ca.* 0.48 eV (11.0 kcal mol^{-1}) is predicted, whose value is similar to that estimated in the case of **C1** (10 kcal mol^{-1}). On a thermodynamic basis, the final H_2 release is negligibly endergonic for **C3** (+0.01 eV, +0.23 kcal mol^{-1}), while a larger ΔG was calculated for **C1** (*ca.* +0.13 eV, +3 kcal mol^{-1}).[27] We should note that **C3** could also follow a different pathway implying the formation of H_2 through reaction of the pyridyl OH group with cobalt-hydride species (**Co(II)H-BPY1H** in Fig. ES26,† H···H distance of 1.56 Å). Nevertheless, although it is closer in distance, such a reaction would lead to an unstable deprotonated OH group and is thus not feasible (Fig. ES24†).

Akin to what was observed for the parent complex **C1** and the other substituted analogues, mechanistic analysis of catalytic hydrogen evolution by complexes **C2** and **C3** still suggests the important role of the hexadentate polypyridine ligand wherein pendant pyridine moieties in the reduced state(s) of the catalyst act as proton relays favouring hydrogen elimination *via* intramolecular routes.

We believe that this ability represents a peculiar figure-of-merit of this class of molecular catalysts, resulting in enhanced catalysis rates over molecular analogues.[23]

4. Conclusions

In conclusion, we have reported here a series of new polypyridyl cobalt complexes introducing $-CO_2^-$, $-CH_2OH$ and –OH *ortho* to the nitrogen of the pyridine group. Surprisingly, **C2** and **C3** display a heptacoordinate structure with the seventh coordination site directly occupied by the ligand. Electrochemical studies in acetonitrile using TFA as the proton donor confirm the ability of all complexes to act as molecular catalysts for the hydrogen evolution reaction with complex **C3** displaying the highest catalysis rate. Photochemical studies under homogeneous conditions in aqueous solution confirmed improved performances for catalyst **C3**. The experimental electrochemical data, supported by DFT calculations, point for all complexes towards an ECEC catalytic mechanism which, in the case of both **C2** and **C4**, requires an initial ligand protonation to trigger catalysis according to a (C)ECEC mechanism. DFT computations further support the important role of the chelating ligand in providing an internal proton relay to assist the hydrogen elimination *via* intramolecular proton transfer processes, thus showcasing a fundamental requisite to achieve sustained catalysis rates using polypyridine cobalt complexes.

Author contributions

FL and AR designed the molecules. FL synthesized the molecules and performed photochemical H_2 evolution studies. FD and MN performed transient absorption spectroscopy. FL, JF, AM and VA performed electrochemical investigations. ES and RS collected and resolved X-ray crystal structures. MM and MP performed computational studies. FL and AR wrote the first draft and MM, MP, MN, and VA collaborated in the finalization of the manuscript.

Conflicts of interest

There are no conflicts to declare.

Acknowledgements

This work received funding from the Swiss National Foundation (Grant 159716, FN 7359) and French National Research Agency (Labex ARCANE, CBH-EUR-GS, ANR-17-EURE-0003). MN acknowledges the University of Ferrara (FIR2021, FAR2022) for funding. Computational resources from the mésocentre EXPLOR of Université de Lorraine (Project 2018CPMXX0602) are acknowledged.

Notes and references

1 V. Balzani, A. Credi and M. Venturi, *Curr. Opin. Chem. Biol.*, 1997, **1**, 506–513.
2 N. S. Lewis and D. G. Nocera, *Proc. Natl. Acad. Sci. U. S. A.*, 2006, **103**, 15729–15735.
3 W. T. Eckenhoff, W. R. McNamara, P. Du and R. Eisenberg, *Biochim. Biophys. Acta Bioenerg.*, 2013, **1827**, 958–973.
4 H. B. Gray and A. W. Maverick, *Science*, 1981, **214**, 1201–1205.
5 V. Balzani, A. Credi and M. Venturi, *ChemSusChem*, 2008, **1**, 26–58.
6 E. S. Andreiadis, M. Chavarot-Kerlidou, M. Fontecave and V. Artero, *Photochem. Photobiol.*, 2011, **87**, 946–964.
7 G. Segev, J. Kibsgaard, C. Hahn, Z. J. Xu, W.-H. Cheng, T. G. Deutsch, C. Xiang, J. Z. Zhang, L. Hammarström, D. G. Nocera, A. Z. Weber, P. Agbo, T. Hisatomi, F. E. Osterloh, K. Domen, F. F. Abdi, S. Haussener, D. J. Miller, S. Ardo, P. C. McIntyre, T. Hannappel, S. Hu, H. Atwater, J. M. Gregoire, M. Z. Ertem, I. D. Sharp, K.-S. Choi, J. S. Lee, O. Ishitani, J. W. Ager, R. R. Prabhakar, A. T. Bell, S. W. Boettcher, K. Vincent, K. Takanabe, V. Artero, R. Napier, B. R. Cuenya, M. T. M. Koper, R. Van De Krol and F. Houle, *J. Phys. D: Appl. Phys.*, 2022, **55**, 323003.
8 S. Berardi, S. Drouet, L. Francàs, C. Gimbert-Suriñach, M. Guttentag, C. Richmond, T. Stoll and A. Llobet, *Chem. Soc. Rev.*, 2014, **43**, 7501–7519.
9 M. Grätzel, *Nature*, 2001, **414**, 338–344.
10 M. Grätzel, *Inorg. Chem.*, 2005, **44**, 6841–6851.
11 V. S. Thoi, Y. Sun, J. R. Long and C. J. Chang, *Chem. Soc. Rev.*, 2013, **42**, 2388–2400.
12 W. T. Eckenhoff, *Coord. Chem. Rev.*, 2018, **373**, 295–316.
13 P. Du and R. Eisenberg, *Energy Environ. Sci.*, 2012, **5**, 6012–6021.
14 D. Brazzolotto, L. K. Wang, H. Tang, M. Gennari, N. Queyriaux, C. Philouze, S. Demeshko, F. Meyer, M. Orio, V. Artero, M. B. Hall and C. Duboc, *ACS Catal.*, 2018, **8**, 10658–10667.

15 T. Straistari, J. Fize, S. Shova, M. Réglier, V. Artero and M. Orio, *ChemCatChem*, 2017, **9**, 2262–2268.

16 D. Brazzolotto, M. Gennari, N. Queyriaux, T. R. Simmons, J. Pecaut, S. Demeshko, F. Meyer, M. Orio, V. Artero and C. Duboc, *Nat. Chem.*, 2016, **8**, 1054–1060.

17 D. Streich, Y. Astuti, M. Orlandi, L. Schwartz, R. Lomoth, L. Hammarström and S. Ott, *Chem.–Eur. J.*, 2010, **16**, 60–63.

18 M. Razavet, V. Artero and M. Fontecave, *Inorg. Chem.*, 2005, **44**, 4786–4795.

19 C. Baffert, V. Artero and M. Fontecave, *Inorg. Chem.*, 2007, **46**, 1817–1824.

20 X. Hu, B. M. Cossairt, B. S. Brunschwig, N. S. Lewis and J. C. Peters, *Chem. Commun.*, 2005, 4723–4725.

21 O. Pantani, E. Anxolabéhère-Mallart, A. Aukauloo and P. Millet, *Electrochem. Commun.*, 2007, **9**, 54–58.

22 V. Artero, M. Chavarot-Kerlidou and M. Fontecave, *Angew. Chem., Int. Ed.*, 2011, **50**, 7238–7266.

23 F. Droghetti, F. Lucarini, A. Molinari, A. Ruggi and M. Natali, *Dalton Trans.*, 2022, **51**, 10658–10673.

24 N. Queyriaux, R. T. Jane, J. Massin, V. Artero and M. Chavarot-Kerlidou, *Coord. Chem. Rev.*, 2015, **304**, 3–19.

25 D. Z. Zee, T. Chantarojsiri, J. R. Long and C. J. Chang, *Acc. Chem. Res.*, 2015, **48**, 2027–2036.

26 F. Lucarini, M. Pastore, S. Vasylevskyi, M. Varisco, E. Solari, A. Crochet, K. M. Fromm, F. Zobi and A. Ruggi, *Chem.–Eur. J.*, 2017, **23**, 6768–6771.

27 F. Lucarini, J. Fize, A. Morozan, M. Marazzi, M. Natali, M. Pastore, V. Artero and A. Ruggi, *Sustain. Energy Fuels*, 2020, **4**, 589–599.

28 M. Nippe, R. S. Khnayzer, J. A. Panetier, D. Z. Zee, B. S. Olaiya, M. Head-Gordon, C. J. Chang, F. N. Castellano and J. R. Long, *Chem. Sci.*, 2013, **4**, 3934–3945.

29 S. Schnidrig, C. Bachmann, P. Muller, N. Weder, B. Spingler, E. Joliat-Wick, M. Mosberger, J. Windisch, R. Alberto and B. Probst, *ChemSusChem*, 2017, **10**, 4570–4580.

30 F. Lucarini, D. Bongni, P. Schiel, G. Bevini, E. Benazzi, E. Solari, F. Fadaei-Tirani, R. Scopelliti, M. Marazzi, M. Natali, M. Pastore and A. Ruggi, *ChemSusChem*, 2021, **14**, 1874–1885.

31 A. Orlando, F. Lucarini, E. Benazzi, F. Droghetti, A. Ruggi and M. Natali, *Molecules*, 2022, **27**, 8277.

32 C. H. Lee, D. K. Dogutan and D. G. Nocera, *J. Am. Chem. Soc.*, 2011, **133**, 8775–8777.

33 M. Natali, E. Badetti, E. Deponti, M. Gamberoni, F. A. Scaramuzzo, A. Sartorel and C. Zonta, *Dalton Trans.*, 2016, **45**, 14764–14773.

34 C. Costentin and J. M. Saveant, *ChemElectroChem*, 2014, **1**, 1226–1236.

35 V. Artero and J. M. Saveant, *Energy Environ. Sci.*, 2014, **7**, 3808–3814.

36 C. Costentin, S. Drouet, M. Robert and J. M. Saveant, *J. Am. Chem. Soc.*, 2012, **134**, 11235–11242.

37 J. T. Muckerman and E. Fujita, *Chem. Commun.*, 2011, **47**, 12456–12458.

38 C. P. Kelly, C. J. Cramer and D. G. Truhlar, *J. Phys. Chem. B*, 2007, **111**, 408–422.

39 J. E. Bartmess, *J. Phys. Chem.*, 1994, **98**, 6420–6424.

40 C. Adamo and V. Barone, *J. Chem. Phys.*, 1999, **110**, 6158–6170.

41 E. Cancès, B. Mennucci and J. Tomasi, *J. Chem. Phys.*, 1997, **107**, 3032–3041.

42 G. W. Trucks, H. B. Schlegel, G. E. Scuseria, M. A. Robb, J. R. Cheeseman, G. Scalmani, V. Barone, G. A. Petersson, H. Nakatsuji, X. Li, M. Caricato, A. V. Marenich, J. Bloino, B. G. Janesko, R. Gomperts, B. Mennucci, H. P. Hratchian, J. V. Ortiz, A. F. Izmaylov, J. L. Sonnenberg, D. Williams-Young, F. Ding, F. Lipparini, F. Egidi, J. Goings, B. Peng, A. Petrone, T. Henderson, D. Ranasinghe, V. G. Zakrzewski, J. Gao, N. Rega, G. Zheng, W. Liang, M. Hada, M. Ehara, K. Toyota, R. Fukuda, J. Hasegawa, M. Ishida, T. Nakajima, Y. Honda, O. Kitao, H. Nakai, T. Vreven, K. Throssell, J. A. Montgomery Jr, J. E. Peralta, F. Ogliaro, M. J. Bearpark, J. J. Heyd, E. N. Brothers, K. N. Kudin, V. N. Staroverov, T. A. Keith, R. Kobayashi, J. Normand, K. Raghavachari, A. P. Rendell, J. C. Burant, S. S. Iyengar, J. Tomasi, M. Cossi, J. M. Millam, M. Klene, C. Adamo, R. Cammi, J. W. Ochterski, R. L. Martin, K. Morokuma, O. Farkas, J. B. Foresman, and D. J. Fox, *Gaussian 16 Revision C.01*, Gaussian, Inc., Wallingford CT, 2016.

43 K. De Buysser, G. G. Herman, E. Bruneel, S. Hoste and I. Van Driessche, *Chem. Phys.*, 2005, **315**, 286–292.

44 C. Fujisue, T. Kadoya, T. Higashino, R. Sato, T. Kawamoto and T. Mori, *RSC Adv.*, 2016, **6**, 53345–53350.

45 L. Forlani, G. Cristoni, C. Boga, P. E. Todesco, E. D. Vecchio, S. Selva and M. Monari, *ARKIVOC*, 2002, **2002**, 198–215.

46 C. Costentin and J.-M. Savéant, *ChemElectroChem*, 2014, **1**, 1226–1236.

47 C.-B. Li, A. J. Bagnall, D. Sun, J. Rendon, M. Koepf, S. Gambarelli, J.-M. Mouesca, M. Chavarot-Kerlidou and V. Artero, *Sustain. Energy Fuels*, 2022, **6**, 143–149.

48 V. Fourmond, P. A. Jacques, M. Fontecave and V. Artero, *Inorg. Chem.*, 2010, **49**, 10338–10347.

49 E. Deponti and M. Natali, *Dalton Trans.*, 2016, **45**, 9136–9147.

50 M. Natali, *ACS Catal.*, 2017, **7**, 1330–1339.

51 R. S. Khnayzer, V. S. Thoi, M. Nippe, A. E. King, J. W. Jurss, K. A. El Roz, J. R. Long, C. J. Chang and F. N. Castellano, *Energy Environ. Sci.*, 2014, **7**, 1477–1488.

52 W. M. Singh, M. Mirmohades, R. T. Jane, T. A. White, L. Hammarström, A. Thapper, R. Lomoth and S. Ott, *Chem. Commun.*, 2013, **49**, 8638–8640.

53 A. Lewandowska-Andralojc, T. Baine, X. Zhao, J. T. Muckerman, E. Fujita and D. E. Polyansky, *Inorg. Chem.*, 2015, **54**, 4310–4321.

54 B. N. DiMarco, D. E. Polyansky, D. C. Grills, P. Wang, Y. Kuwahara, X. Zhao and E. Fujita, *ChemPhysChem*, 2021, **22**, 1478–1487.

55 N. Queyriaux, E. Giannoudis, C. D. Windle, S. Roy, J. Pécaut, A. G. Coutsolelos, V. Artero and M. Chavarot-Kerlidou, *Sustain. Energy Fuels*, 2018, **2**, 553–557.

56 V. D. Parker, K. L. Handoo, F. Roness and M. Tilset, *J. Am. Chem. Soc.*, 1991, **113**, 7493–7498.

57 S. Grau, M. Schilling, D. Moonshiram, J. Benet-Buchholz, S. Luber, A. Llobet and C. Gimbert-Suriñach, *ChemSusChem*, 2020, **13**, 2745–2752.